



## Using Semicircular Sampling to Increase Sea Water/Ice Discrimination Altitude

Alexey Nekrasov<sup>1, 2\*</sup> , Alena Khachaturian<sup>1</sup> , Colin Fidge<sup>3</sup> 

<sup>1</sup> Department of Radio Engineering Systems, Saint Petersburg Electrotechnical University, 197022 Saint Petersburg, Russia.

<sup>2</sup> Institute for Computer Technologies and Information Security, Southern Federal University, 347922 Taganrog, Russia.

<sup>3</sup> Faculty of Science, Queensland University of Technology (QUT), Gardens Point Campus, Brisbane, QLD 4001, Australia.

### Abstract

The rapid development of aircraft and unmanned aerial vehicles (UAV) increases their use, including in polar areas, which are characterized by their remoteness and rather harsh conditions. The dominant trends in airborne radar development are expanding their functionality and increasing the altitude of their applicability. Our study focuses on the functionality enhancement of airborne high-altitude conical scanning radars currently used for circular clouds and precipitation observations as well as for sea wind measurements. Recently, we showed how a semicircular observation scheme, instead of a circular one, can double the maximum applicable altitude of sea wind measurements made with such radars. Here we apply this approach to show how an airborne high-altitude conical scanning radar's functionality can also be expanded for sea water/ice discrimination within a semicircular observation scheme, again doubling the maximum discrimination altitude compared to circular observations. The discrimination is performed in scatterometer mode using the minimum statistical distance of the measured normalized radar cross sections (NRCSs) to the geophysical model functions (GMFs) of the sea water and ice underlying surfaces. However, as no sea ice GMF is available for the considered horizontal transmit and receive polarization at the Ku band, we instead used a substitute sea ice GMF having the same azimuth isotropic property setting for its NRCSs as the averaged value of the measured azimuth NRCSs within the semicircular observations scheme. Our analysis found that incidence angles of 30°, 45°, and 60° are well suited to our sea water/ice discrimination method, and that incidence angles higher than 30° are preferable as they provide a higher difference in the statistical distance of the measured NRCSs to the sea ice and water GMFs, whereas an incidence angle of 30° provides the highest applicable altitude for sea water/ice discrimination and wind retrieval. We also demonstrated the ability of the sea water/ice discrimination procedure's implementation for any airborne wind scatterometer or multimode radar operated in scatterometer mode over freezing seas to avoid entirely erroneous sea wind measurement results when a sea ice surface is observed. The obtained results can also be used for enhancing aircraft and UAV radars and for developing new remote sensing systems.

### Keywords:

UAV;  
Remote Sensing;  
Airborne Scatterometer;  
Radar Backscatter;  
Sea Water/Ice Discrimination.

### Article History:

<b>Received:</b>	23	December	2023
<b>Revised:</b>	12	March	2024
<b>Accepted:</b>	18	March	2024
<b>Published:</b>	01	April	2024

## 1- Introduction

Sea ice as well as wind and wave measurements are important parts of environmental monitoring and safe navigation, including over freezing seas [1–3]. For that purpose, various space-borne sensors have been used as the main observers to provide global, nonstop observations for four decades [4]. At the same time, auxiliary observations from shore stations, specially designed buoys, ships, and aircraft are also used as a local complement to improve global measurements by synergy of the various measurement instruments [1, 5].

\* **CONTACT:** alexei-nekrassov@mail.ru

**DOI:** <http://dx.doi.org/10.28991/ESJ-2024-08-02-07>

© 2024 by the authors. Licensee ESJ, Italy. This is an open access article under the terms and conditions of the Creative Commons Attribution (CC-BY) license (<https://creativecommons.org/licenses/by/4.0/>).

The rapid development of aircraft and then unmanned aerial vehicles (UAV) allowed them to be used more and more actively, including in polar areas, which are characterized by their remoteness and rather harsh conditions. The development of UAV remote sensing generated new ideas and technologies, realizing their advantages in efficient, safe, and low-cost marine monitoring [6]. Originally, the first UAVs and their instruments were not for remote sensing applications, but now remote sensing instruments have been adopted or specially designed for use on UAVs, including in the marine domain, and so UAVs are becoming the newest observation platform with high mobility, flexibility, efficiency, and low-cost performance [7]. They can be equipped with a number of instruments, depending on their needs and observation requirements. In this regard, it is important to expand the functionality of the installed remote sensing equipment and increase the flight duration and altitude range of the aerial vehicles [8, 9].

An example of such a remote sensing instrument is the High-Altitude Imaging Wind and Rain Airborne Profiler (HIWRAP). This is an airborne conical scanning radar designed for NASA's (National Aeronautics and Space Administration) high-altitude Global Hawk UAV with a service ceiling of about 20 km [10–12]. It was created to estimate atmospheric winds, tracing clouds and precipitation, retrieve sea wind vectors as a wind scatterometer, and perform 3D mapping of winds and precipitation.

A circular observation scheme is frequently used for airborne sea wind measurements by scatterometers or radars with a scatterometer mode [10, 12–15]. This scheme supports normalized radar cross sections (NRCSs) of the underlying surface with an entire azimuth observation from  $0^\circ$  to  $360^\circ$  at an incidence angle of interest that reveals its azimuthal features and enables reliable sea wind retrieval using an appropriate sea water geophysical model function (GMF) [12, 13, 15]. In previous research, we evaluated sea wind retrieval capability with a circular measurement scheme at incidence angles of  $30^\circ$  to  $60^\circ$  by airborne rotating beam scatterometers in rectilinear flight [16–18] and in circular flight by an FM-CW (Frequency Modulated Continuous Wave) millimeter wave demonstrator system [19], Doppler navigation system [20, 21], and airborne weather radar [22, 23]. These earlier studies proved the feasibility of the circular observation scheme for retrieval of sea surface winds by airborne scatterometer instruments and the scheme's applicability. However, despite the variety of such airborne scatterometer instruments available nowadays, the application of a circular observation scheme has the same altitude restrictions for them all due to their observation geometry, which assumes the observed area's diameter should not surpass 15–20 km in accordance with the expectation of homogeneous wave and wind conditions in such an area. For this reason, the maximum altitude limitations are about 17.3, 10, and 5.77 km at incidence angles of  $30^\circ$ ,  $45^\circ$ , and  $60^\circ$ , respectively [16].

Current trends in airborne radar development are not only in expanding their functionality and integrating their instruments and systems, but also in increasing the maximum altitude of their applicability. Modern manned and unmanned propeller and turbojet aircraft can operate above 20,000 and even 30,000 m [24, 25]. This, in turn, requires ensuring the radars' operability at these higher altitudes too. In this connection, we recently considered how to use a semicircular measurement scheme instead of typical circular observations for sea wind measurements with a conical scanning radar to increase the maximum altitude of its applicability. We demonstrated the potential to double the maximum altitude of the wind recovery method using a semicircular measurement scheme compared to a circular measurement scheme [26, 27]. As sea wind retrieval is an integral part of the sea water/ice discrimination procedure, we therefore conjectured that a semicircular observation scheme should also significantly increase the maximum possible altitude of sea water/ice discrimination.

In addition to increasing the maximum altitude of the sea wind retrieval method, it is also of great interest to enhance the high-altitude conical scanning radar's functionality to allow sea water/ice discrimination when the radar operates over freezing seas, in addition to the typical application of HIWRAP for estimating atmospheric winds by tracing clouds and precipitation, retrieval of the wind vector over water, and performing wind and precipitation 3D mapping. For this purpose, we consider here a sea water/ice discrimination method that is based on a significantly different azimuth shape of the water and sea ice NRCSs. Previously, we demonstrated the feasibility of the method for airborne weather radar [28] and satellite-based scatterometers [29, 30]. The decision on whether sea water or ice is observed is made based on the minimum statistical distance, within the observation scheme, of the measured NRCSs to the sea ice and water GMFs. Currently, however, no high-altitude conical scanning radar can provide sea wind and ice measurements in scatterometer mode.

Therefore, in this article, we evaluate the potential for sea water/ice discrimination within a semicircular NRCS observation scheme by an airborne high-altitude conical scanning radar, both to expand the radar's functionality and to increase the maximum altitude of the sea water/ice discrimination method's applicability compared to a conventional circular observation scheme.

## 2- Material and Methods

In this research, we consider azimuth NRCS sampling, sea water/ice discrimination, and the possibility of increasing the maximum altitude of sea water/ice discrimination with regard to a high-altitude conical scanning radar. The conical scanning radar operates in scatterometer mode. A minimum statistical distance of the measured NRCSs to the sea water and ice GMFs is used for the sea water/ice discrimination. Since a suitable sea ice GMF is not available, it is substituted by an azimuth isotropic line with a value of the averaged measured azimuth NRCSs. The semicircular observation scheme is used to increase the maximum altitude of sea water/ice discrimination.

Verification of this approach is performed with the help of simulations. The sea water surface case and the sea ice surface case are considered. For that purpose, we use the right-side NRCS semicircle (Figure 1) with azimuths from 0° to 180°, presented by  $N = 37$  azimuth sectors of 5° width, with the generation of 261 “measured” NRCSs and their integration for each azimuth sector. A Rayleigh Power (Exponential) distribution along with the sea water and ice GMFs and an assumption of 0.2 dB instrument noise are used to generate “measured” sea water and ice NRCSs. Simulations are performed for incidence angles of 30°, 45°, and 60° at wind speeds of 2, 10, 20, and 30 m/s.

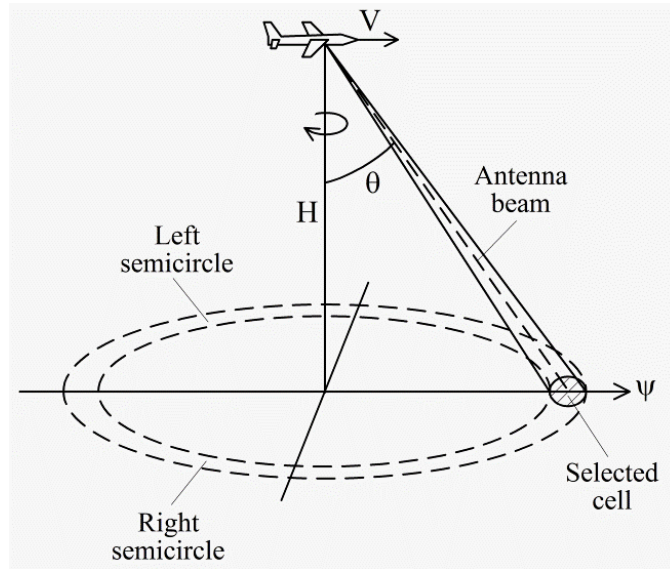


**Figure 1. Conical scanning radar geometry: V is the current speed of flight; H is the altitude;  $\theta$  is the incidence angle; and  $\psi$  is the flight direction**

The decision about which surface is observed is made in accordance with a sea water/ice discrimination criterion. This criterion is based on two parameters. If the statistical distance of the measured NRCSs to the sea water GMF is less than the statistical distance of the measured NRCSs to the sea ice GMF then a water surface is observed, otherwise an ice surface is observed. However, if these statistical distances are approximately equal, there may be some uncertainty about the discrimination result; a helpful indicator of discrimination reliability is the ratio of the two statistical distances.

**2-1-Conical Scanning and Sea Wind Retrieval**

Conical scanning is in demand not only for a number of current and future space-borne scatterometers, but also for airborne scatterometers and maritime/ground surveillance multimode radars with a scatterometer mode. The generalized geometry of the airborne conical scanning radar is presented in Figure 1. Conical scanning allows circular sampling of azimuth NRCSs of the surface at an appropriate incidence angle  $\theta$ . Such a conical observation is beneficial for sea surface observations when the near-surface wind vector is measured. To retrieve the wind vector from the measured azimuth NRCSs, a sea water GMF designed for wind detection over water is used. Recently, we have demonstrated how it can be advantageous when the following system of equations, composed for azimuth NRCSs, is used for wind retrieval using various scatterometer instruments [16–18, 26, 27, 31]:

$$\begin{cases} \sigma_1^{**} = GMF(\theta, \psi_1) \\ \sigma_2^{**} = GMF(\theta, \psi_2) \\ \dots \dots \dots \\ \sigma_i^{**} = GMF(\theta, \psi_i) \\ \dots \dots \dots \\ \sigma_{N-1}^{**} = GMF(\theta, \psi_{N-1}) \\ \sigma_N^{**} = GMF(\theta, \psi_N) \end{cases} \quad (1)$$

where  $\sigma_i^{**}$  is the  $i^{th}$ -measured NRCS, related to azimuth sector number  $i$  with azimuth direction  $\psi_i$  relative to the flight direction of the aircraft  $\psi$ ;  $\psi_1 = 0^\circ$  if counting starts from the flight direction. The observed NRCS curve is composed of  $N$  azimuth sectors with each sector of azimuth width  $\Delta\alpha_s$ . Thus, the number of observed sectors (the number of equations in System of Equations 1) depends on the observation scheme and azimuth sector width. The sector number is in the range  $i = \overline{1, N}$ , and  $N = 360^\circ / \Delta\alpha_s$  in a circular observation scheme (when the whole 360° circular NRCS curve is obtained), but  $N = 180^\circ / \Delta\alpha_s + 1$  in a semicircular observation scheme (when a half of the whole 360° circular NRCS curve is obtained). For example, if the azimuth sector has a 5° width, the corresponding circular observation scheme consists of 72 sectors, while the semicircular observation scheme (the right or left semicircle in Figure 1) has 37 sectors only.

If a water surface is observed, the  $i^{\text{th}}$ -measured NRCS  $\sigma^\circ(U, \theta, \alpha + \psi_i)$  can be presented as dependent on the wind speed  $U$ , incidence angle  $\theta$ , azimuth angle  $\alpha$  (the upwind direction corresponds to  $\alpha = 0^\circ$ ), and azimuth direction of the sector  $\psi_i$  observed relative to the aircraft's flight direction  $\psi$  in accordance with the appropriate sea water GMF, as in the following equation [32]:

$$\sigma^\circ(U, \theta, \alpha + \psi_i) = A(U, \theta) + B(U, \theta) \cos(\alpha + \psi_i) + C(U, \theta) \cos(2(\alpha + \psi_i)) \quad (2)$$

where  $A(U, \theta)$ ,  $B(U, \theta)$ , and  $C(U, \theta)$  are the Fourier terms dependent on the wind speed and incidence angle. For example, the coefficients can be presented as  $A(U, \theta) = a_0(\theta)U^{\gamma_0(\theta)}$ ,  $B(U, \theta) = a_1(\theta)U^{\gamma_1(\theta)}$ , and  $C(U, \theta) = a_2(\theta)U^{\gamma_2(\theta)}$ , where

$$\begin{aligned} a_0(\theta) &= 10^{2.47324 - 0.22478\theta + 0.001499\theta^2} \\ a_1(\theta) &= 10^{-0.50593 - 0.11694\theta + 0.000484\theta^2} \\ a_2(\theta) &= 10^{1.63685 - 0.2100488\theta + 0.001383\theta^2} \\ \gamma_0(\theta) &= -0.15 + 0.071\theta - 0.0004\theta^2 \\ \gamma_1(\theta) &= -0.02 + 0.061\theta - 0.0003\theta^2 \\ \gamma_2(\theta) &= -0.16 + 0.074\theta - 0.0004\theta^2 \end{aligned} \quad (3)$$

for a Ku-band GMF at the horizontal transmit and receive polarization [33]. The water GMF defined by Equation 1 is applicable for wind recovery not only for a narrow beam in the horizontal plane or narrow azimuth sector at the NRCS sampling point, but also when the azimuth sector width is up to  $15^\circ$ – $20^\circ$  [34, 35]. Thus, in the case of sea water surface observation, the wind speed and upwind direction can be retrieved using Equations 1 and 2. The upwind direction conversion into navigation wind direction  $\psi_{nav.w}$  is performed with the following equation [36]:

$$\psi_{nav.w} = \psi - \alpha \pm 180^\circ \quad (4)$$

## 2-2-Sea Water/Ice Discrimination Criterion

Although the water surface GMF's shape depends significantly on the azimuth angle (Equation 2) [37], the sea ice GMF's shape is considered as azimuthally isotropic [38–40]. Therefore, this difference in the azimuth shape of the water and sea ice NRCSs can be a key feature to provide sea water/ice discrimination when the underlying surface is observed with the conical scanning scatterometer. To perform sea water/ice discrimination, both the sea water and ice GMFs must be available for the conical scanning radar operated at the appropriate band, transmit and receive polarization. To discriminate between water and sea ice, a method based on the minimum statistical distance of the measured NRCSs to the sea ice and water GMFs has been used in previous research [38].

Recently, we have also shown this method's feasibility for airborne weather radar [28], and satellite-based scatterometers [29, 30]. The C-band sea water and ice GMFs for the vertical transmit and receive polarization [39, 41, 42] were used in those cases. The statistical distance of the measured NRCSs to the water and sea ice GMFs were defined as the following sea water  $S_{\approx}$  and sea ice  $S_{\equiv}$  summation results:

$$S_{\approx} = \sum_{i=1}^N (\sigma_i^{\circ*} - \sigma_{\approx,i}^\circ)^2 \quad (5)$$

$$S_{\equiv} = \sum_{i=1}^N (\sigma_i^{\circ*} - \sigma_{\equiv,i}^\circ)^2 \quad (6)$$

where  $i = \overline{1, N}$ ,  $N$  is the number of azimuth sectors observed at different azimuth directions, and  $\sigma_{\approx,i}^\circ$  and  $\sigma_{\equiv,i}^\circ$  are the sea water and ice GMFs closest to the  $i^{\text{th}}$ -measured NRCS, respectively.

From here, the decision about which kind of surface has been observed can be made using the following criterion:

$$\begin{cases} S_{\approx} < S_{\equiv} \rightarrow \text{water surface observed} \\ S_{\approx} > S_{\equiv} \rightarrow \text{ice surface observed} \\ S_{\approx} \approx S_{\equiv} \rightarrow \text{discrimination uncertainty} \end{cases} \quad (7)$$

## 2-3-Substitution of Unknown Sea Ice GMF

Unfortunately, the sea ice GMF is not always known for the appropriate band, and transmit and receive polarization. Bearing in mind the isotropic character of the sea ice backscattering azimuth shape [39, 40], here we assumed the unknown sea ice GMF to be as follows:

$$\sigma_{\equiv,i}^\circ = \sigma_{\approx,i}^\circ \quad (8)$$

where;

$$\sigma_{\equiv}^\circ = \frac{1}{N} \sum_{i=1}^N \sigma_i^{\circ*} \quad (9)$$

## 2-4-Indicators of Sea Water/Ice Discrimination Reliability

In addition to the absolute values of the sea water and ice summation results, the ratios of the statistical distances can serve as indicators of the discrimination result's reliability. The ratio of the sea ice and water summation results  $\delta_{S_{\approx}/S_{\approx}}$  can be used to determine whether or not the measured semicircular NRCSs are closer to the sea water GMF than to the sea ice GMF in a sea water surface scenario:

$$\delta_{S_{\approx}/S_{\approx}} = \frac{S_{\approx}}{S_{\approx}} \quad (10)$$

while the ratio of the sea water and ice summation results  $\delta_{S_{\approx}/S_{\approx}}$  can be used to determine whether or not the measured semicircular NRCSs are closer to the sea ice GMF than to the sea water GMF in a sea ice surface scenario:

$$\delta_{S_{\approx}/S_{\approx}} = \frac{S_{\approx}}{S_{\approx}} \quad (11)$$

If the value of the corresponding ratio is greater than 1, the discrimination is considered more reliable.

## 2-5-Assumption of Maximum Altitude Increase

Taking into consideration that the maximum altitude of the wind retrieval method with a typical circular observation scheme is about 17.3 km at an incidence angle of  $30^\circ$  and decreases with the incidence angle decrease to 5.77 km at an incidence angle of  $60^\circ$ , here we consider the possibility of sea water/ice discrimination by an airborne high-altitude conical scanning radar with the semicircular observation scheme (the right or left semicircle in Figure 1) to increase the maximum altitude of the method's applicability. As the maximum altitude of the sea wind retrieval method's applicability is doubled when a semicircular observation scheme is applied [26, 27], we expected that this scheme will also be advantageous for sea water/ice discrimination as it will similarly allow an increase in the maximum altitude of the discrimination method when using a high-altitude conical scanning radar.

## 2-6-Methodology Flowchart

The flowchart of our methodology is presented in Figure 2. Following semicircular measurement of radar cross sections, geophysical model functions are calculated for both sea water and sea ice scenarios. The results are summed for both cases and the sea surface is determined by whichever sum is smaller, or an uncertain result is returned if the sums are near equal.

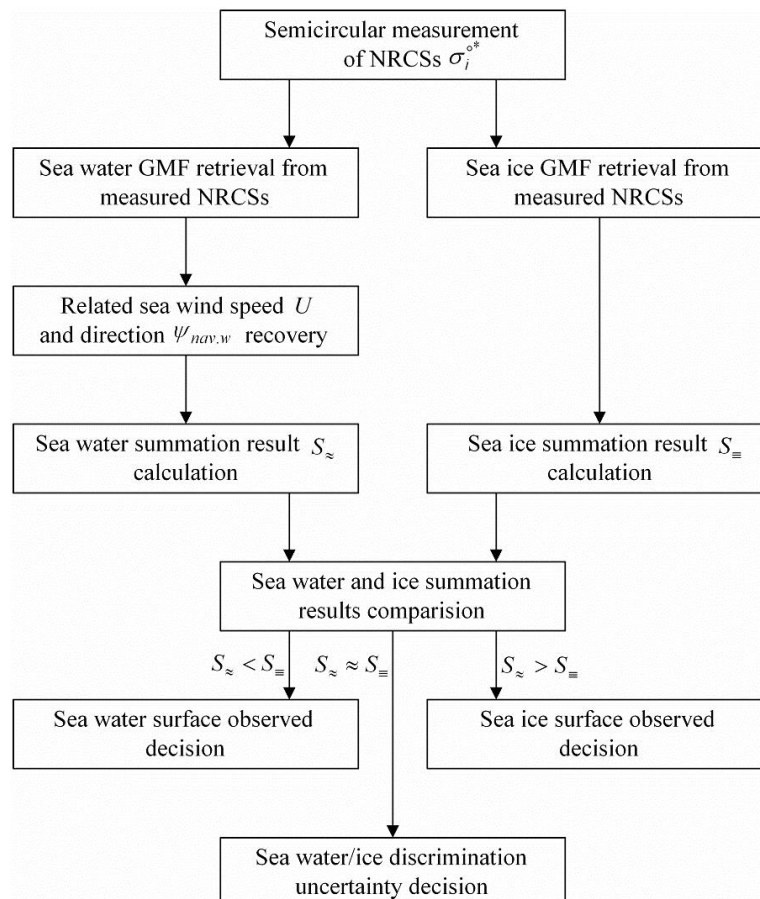


Figure 2. Flowchart of the methodology

### 3- Results and Discussion

In previous work, to verify a wind vector retrieval procedure in the case of a semicircular observation scheme, we performed simulations considering the right-side NRCS semicircle with azimuths from  $0^\circ$  to  $180^\circ$  presented by  $N = 37$  azimuth sectors with a  $5^\circ$  width, generating 261 “measured” NRCSs and integrating them for each azimuth sector [26, 27]. A Rayleigh Power (Exponential) distribution and a sea water GMF by Equations 2 and 3 with an assumption of 0.2 dB instrument noise (currently considered the upper threshold for wind scatterometers) were used. In this paper, we want to similarly verify our sea water/ice discrimination method with semicircular NRCS sampling. Therefore, to be consistent with those previous wind retrieval simulations, here we have used the same given conditions and GMF for the sea water surface case, and in the sea ice surface case, the GMF is provided by Equations 8 and 9.

Circular observations have the advantage of providing all four extrema of the water azimuth’s NRCS curve (consistent with the sea water GMF), but semicircular observations cover only half of the circular NRCS curve, and so only 2 or 3 extrema of the water azimuth’s NRCS curve can be available. Therefore, we consider here the worst case of the semicircular sea water azimuth NRCS curve observation with azimuths from  $90^\circ$  to  $270^\circ$  characterized by the lowest difference of the NRCS values between the second (downwind) maximum and (crosswind) minima of the azimuth’s NRCS curve.

During this study, we simulated two scenarios for the observed underlying surface, a sea water surface and a sea ice surface. The simulations were performed for the three particular incidence angles of  $30^\circ$ ,  $45^\circ$ , and  $60^\circ$  (corresponding to low, medium, and high incidence angles within a plateau region of the Bragg backscattering predominance mostly used by wind scatterometers [13, 43]) at the particular wind speeds of 2, 10, 20, and 30 m/s (corresponding to low, moderate, high, and extreme wind conditions [15, 44]).

#### 3-1-Sea Water Underlying Surface Scenario

The results of the sea water surface case simulations are shown in Figures 3 to 6.

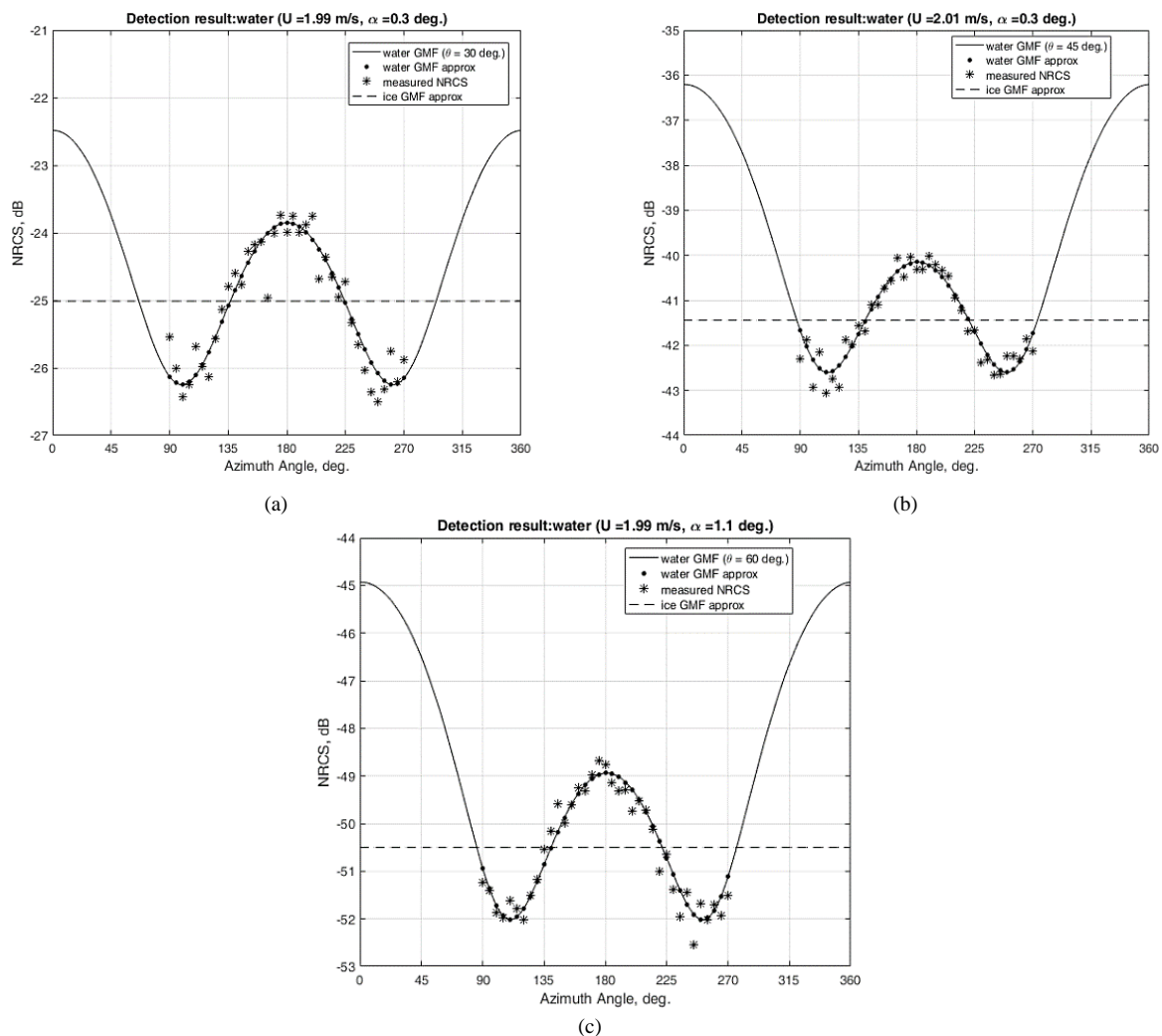


**Figure 3.** Sea water surface simulation results at 2 m/s wind speed and various incidence angles: (a)  $30^\circ$ ; (b)  $45^\circ$ ; (c)  $60^\circ$ ;  $U$  is the wind speed;  $\alpha$  is the upwind direction; and  $\theta$  is the incidence angle

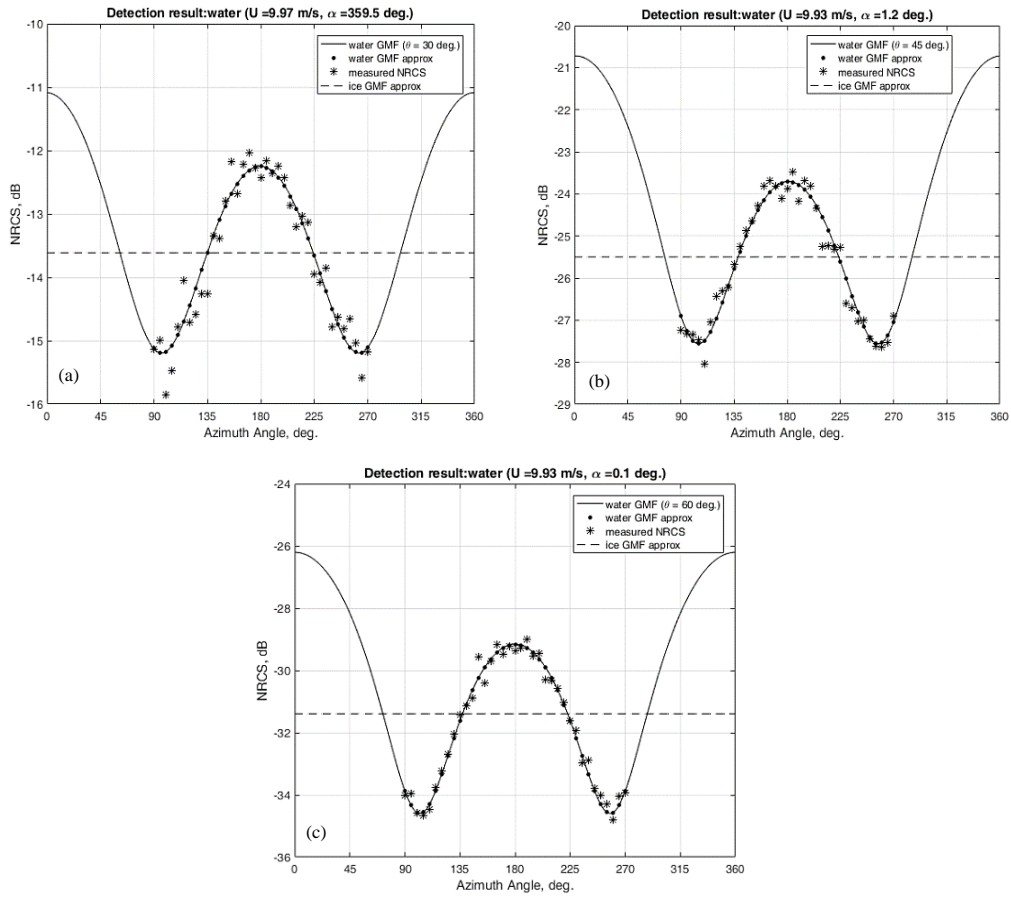


**Figure 4.** Sea water surface simulation results at 10 m/s wind speed and various incidence angles: (a) 30°; (b) 45°; (c) 60°;  $U$  is the wind speed;  $\alpha$  is the upwind direction; and  $\theta$  is the incidence angle

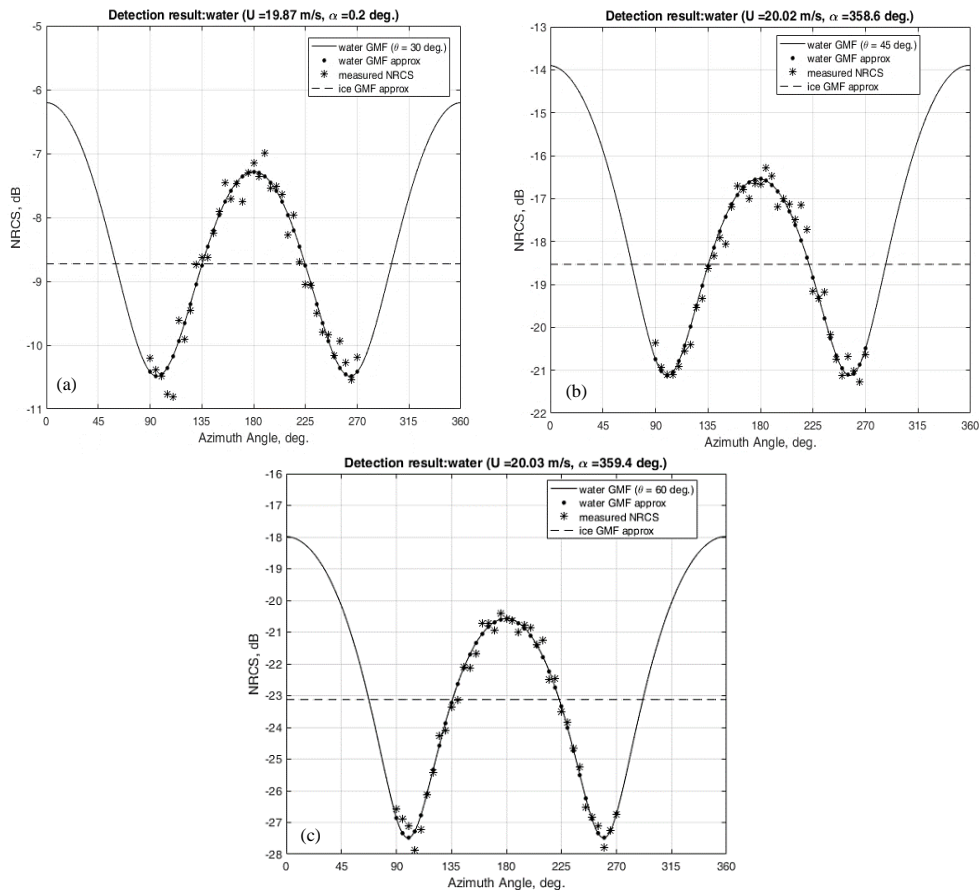


**Figure 5.** Sea water surface simulation results at 20 m/s wind speed and various incidence angles: (a) 30°; (b) 45°; (c) 60°;  $U$  is the wind speed;  $\alpha$  is the upwind direction; and  $\theta$  is the incidence angle

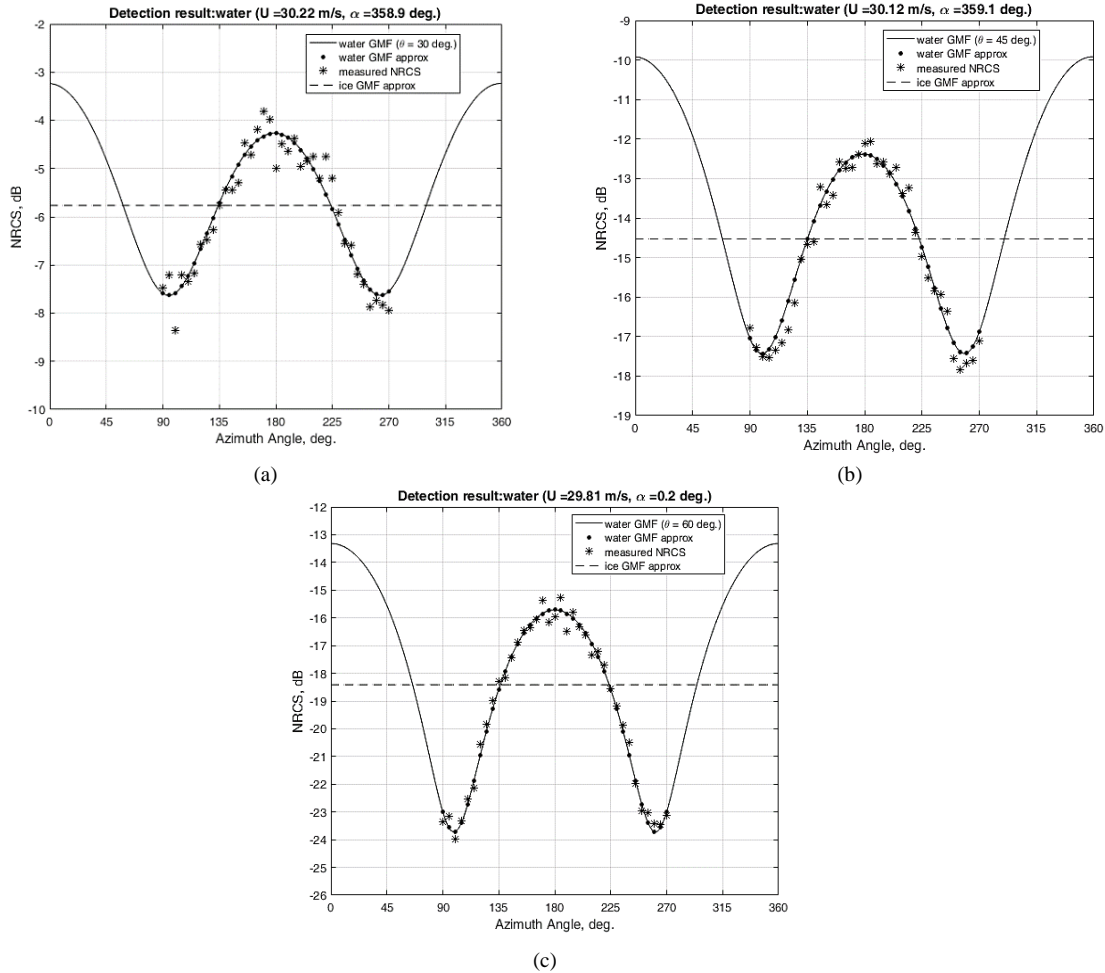


**Figure 6.** Sea water surface simulation results at 30 m/s wind speed and various incidence angles: (a) 30°; (b) 45°; (c) 60°; *U* is the wind speed; *α* is the upwind direction; and *θ* is the incidence angle

The summation results obtained for the sea water surface scenario with the help of Equations 5 and 6 are presented in Table 1. The ratios of the sea ice and water summation results in the water surface scenario, which are the discrimination reliability indicators for us, are given in Table 2.

**Table 1.** Sea water surface scenario summation results

Wind speed	Summation result	Incidence angle		
		30°	45°	60°
2 m/s	$S_{\approx}$	$1.64711 \cdot 10^{-6}$	$6.12467 \cdot 10^{-10}$	$1.0319 \cdot 10^{-11}$
	$S_{=}$	$1.54923 \cdot 10^{-5}$	$9.14969 \cdot 10^{-9}$	$2.08599 \cdot 10^{-10}$
10 m/s	$S_{\approx}$	$2.88278 \cdot 10^{-4}$	$1.14338 \cdot 10^{-6}$	$7.83354 \cdot 10^{-8}$
	$S_{=}$	$4.86866 \cdot 10^{-3}$	$3.27321 \cdot 10^{-5}$	$3.66344 \cdot 10^{-6}$
20 m/s	$S_{\approx}$	$1.74222 \cdot 10^{-3}$	$3.1715 \cdot 10^{-5}$	$3.46813 \cdot 10^{-6}$
	$S_{=}$	$4.8971 \cdot 10^{-2}$	$1.06559 \cdot 10^{-3}$	$2.4877 \cdot 10^{-4}$
30 m/s	$S_{\approx}$	$1.63578 \cdot 10^{-2}$	$2.17555 \cdot 10^{-4}$	$5.27294 \cdot 10^{-5}$
	$S_{=}$	0.22332	$8.84582 \cdot 10^{-3}$	$2.523329 \cdot 10^{-2}$

**Table 2.** Sea ice/water summation results' ratios in the sea water surface scenario

Sea ice/water summation results' ratios	Wind speed	Incidence angle		
		30°	45°	60°
	2 m/s	9.41	14.94	20.22
	10 m/s	16.89	28.63	46.77
	20 m/s	28.11	33.6	71.73
	30 m/s	13.65	40.66	47.85

These graphs show well the closer fit of the “measured” semicircular NRCSs (asterisks in Figures 3 to 6) to the curve of the sea water GMF (solid line) than to the approximated line of the sea ice GMF (dashed line) at the considered speeds of the sea wind and incidence angles in the case of the water surface scenario, and so the underlying surface is correctly recognized as a water surface by the sea water/ice discrimination method via Equation 7. In Table 2, we can see that the sea ice and water summation results’ ratios significantly exceed the value of 1, and they increase with an increasing incidence angle, showing the preferability of incidence angles higher than 30° for sea water/ice discrimination (within the considered incidence angles of 30°, 45°, and 60°). This effect can be explained by an increase in the azimuth anisotropy of water backscattering with an increase in the incidence angle [37].

These figures also indicate that wind retrieval by Equations 1 to 3 is fairly accurate, as the wind measurement errors do not exceed 0.22 m/s and 1.4°. Our previous detailed study of wind retrieval by Equations 1 to 3 within the same semicircular observation scheme and conditions gave maximum wind errors of 0.78 m/s and 5.3° in wind speed ranges of 2–30 m/s [27]. Figure 7 shows the wind recovery maximum errors depending on the incidence angle. Their values demonstrate a slight tendency to decrease with an increasing incidence angle. Thus, we can see that the wind errors always remain within the range of typical wind scatterometer errors of ±2 m/s and ±20° [45], proving the feasibility of the semicircle observation scheme for wind retrieval over the sea surface.

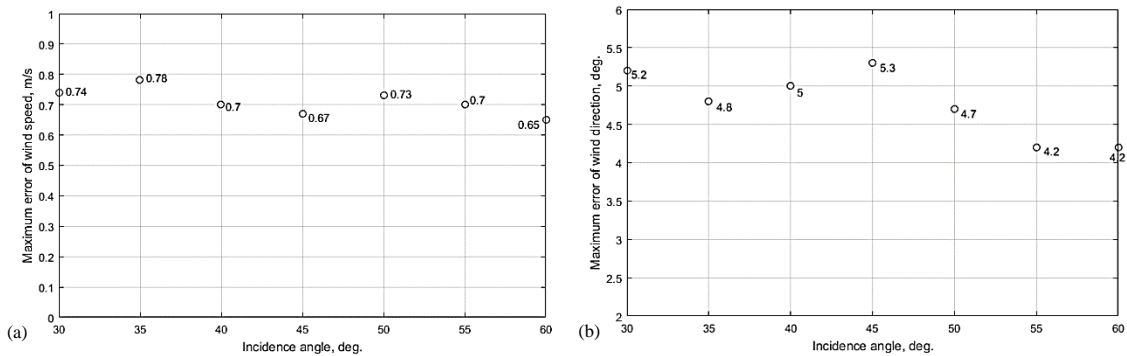


**Figure 7. Sea wind recovery maximum errors in a semicircular scheme based on our previous simulation results [27]: (a) wind speed maximum error; and (b) wind direction maximum error**

### 3-2-Sea Ice Underlying Surface Scenario

Following the sea water-based simulations, we then simulated sea water/ice discrimination within the semicircular scheme in an underlying sea ice scenario. The results of the sea ice surface case simulations are shown in Figures 8-11.

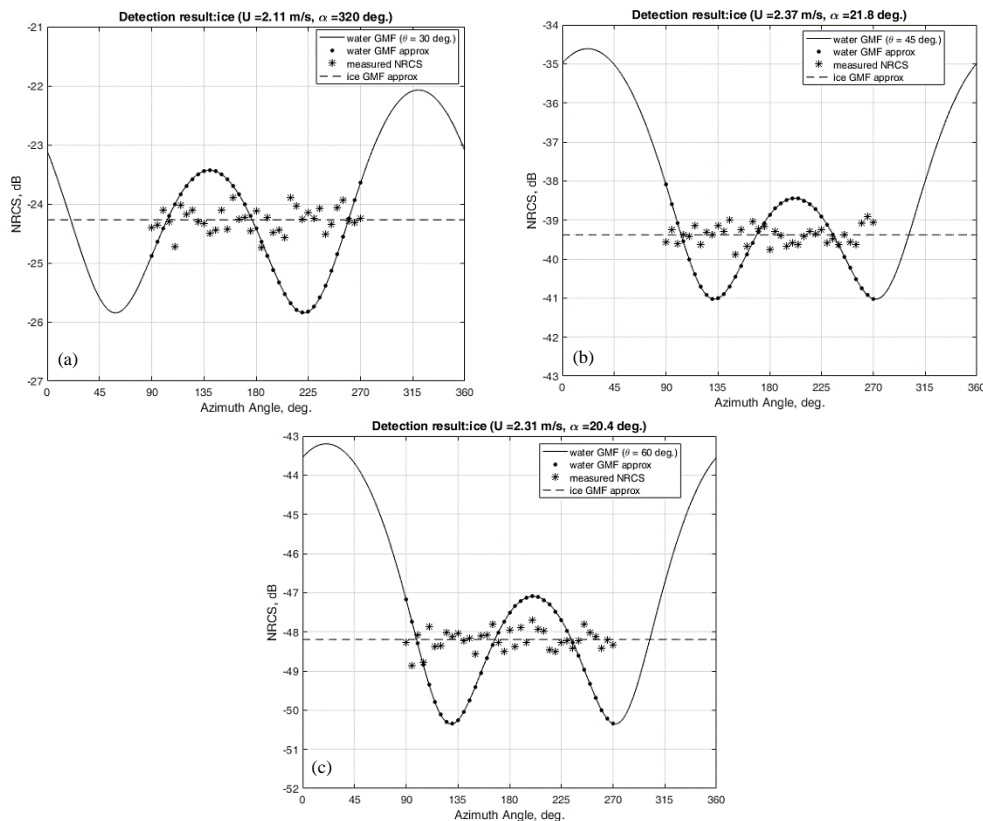


**Figure 8. Sea ice surface simulation results at 2 m/s wind speed and various incidence angles: (a) 30°; (b) 45°; (c) 60°; U is the wind speed;  $\alpha$  is the upwind direction; and  $\theta$  is the incidence angle**

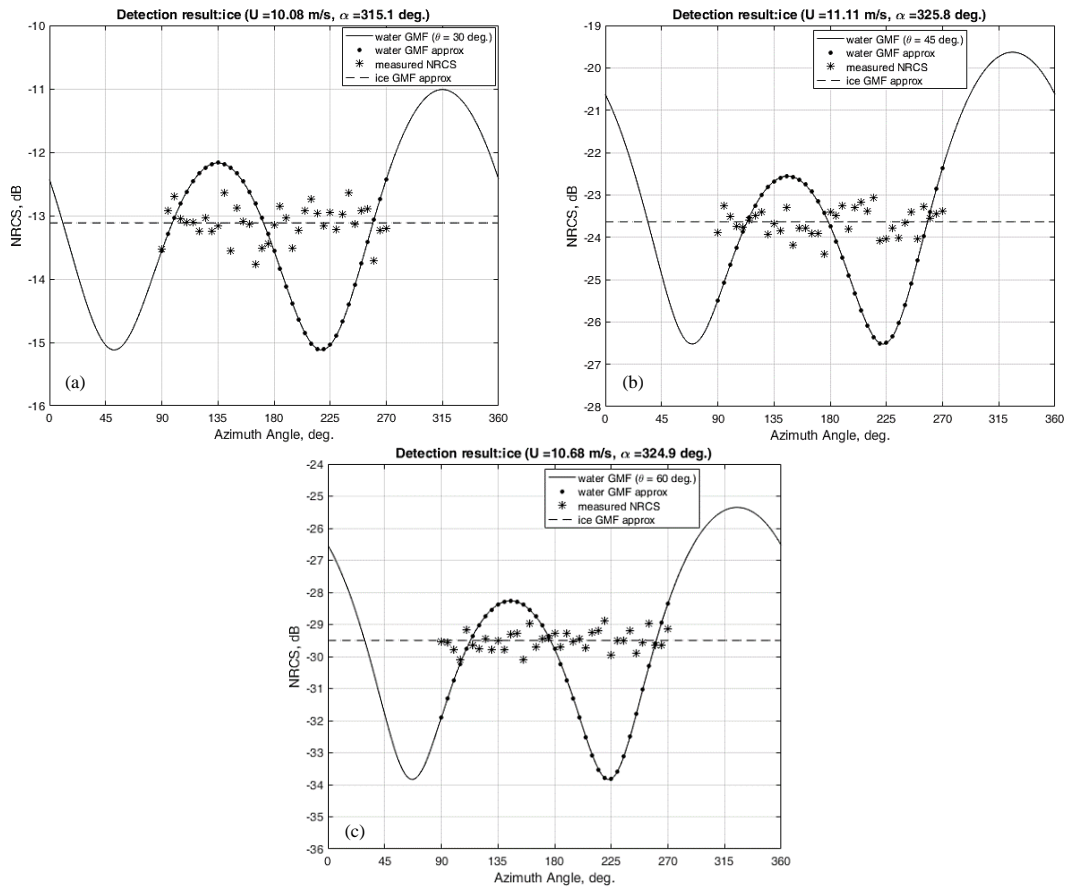


**Figure 9.** Sea ice surface simulation results at 10 m/s wind speed and various incidence angles: (a) 30°; (b) 45°; (c) 60°;  $U$  is the wind speed;  $\alpha$  is the upwind direction; and  $\theta$  is the incidence angle

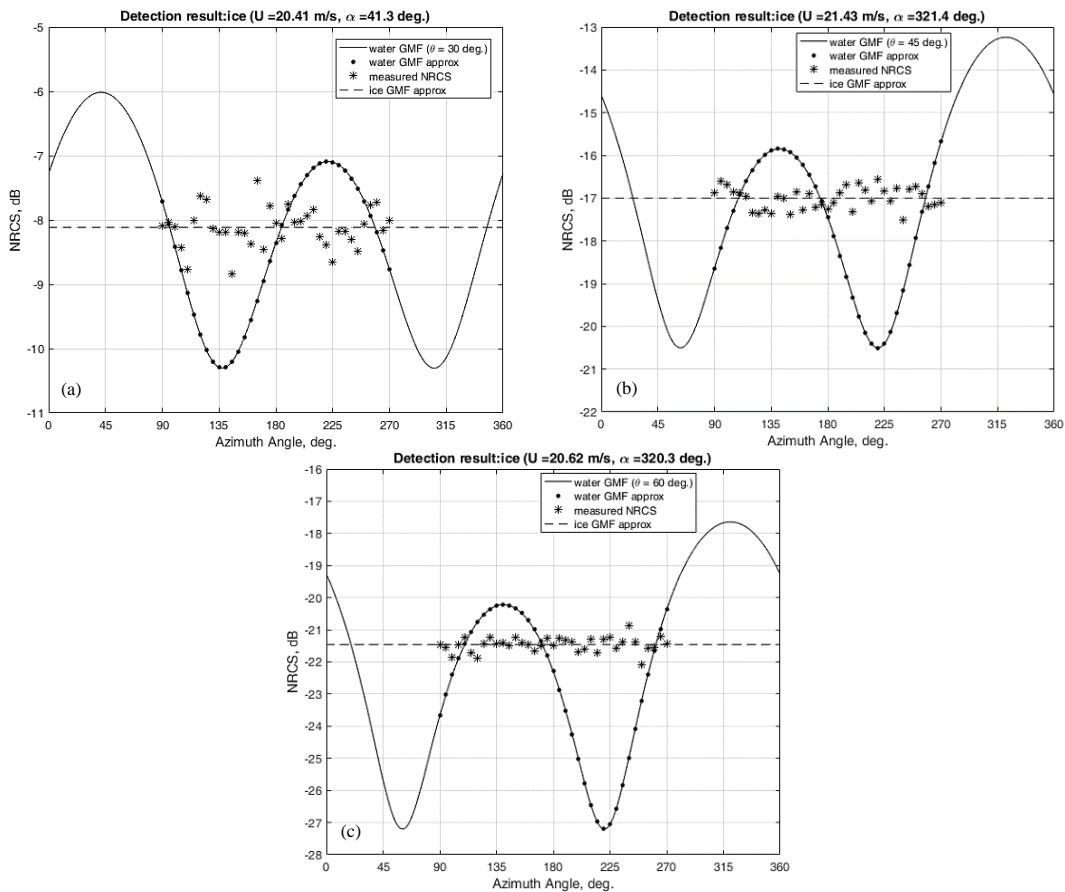


**Figure 10.** Sea ice surface simulation results at 20 m/s wind speed and various incidence angles: (a) 30°; (b) 45°; (c) 60°;  $U$  is the wind speed;  $\alpha$  is the upwind direction; and  $\theta$  is the incidence angle

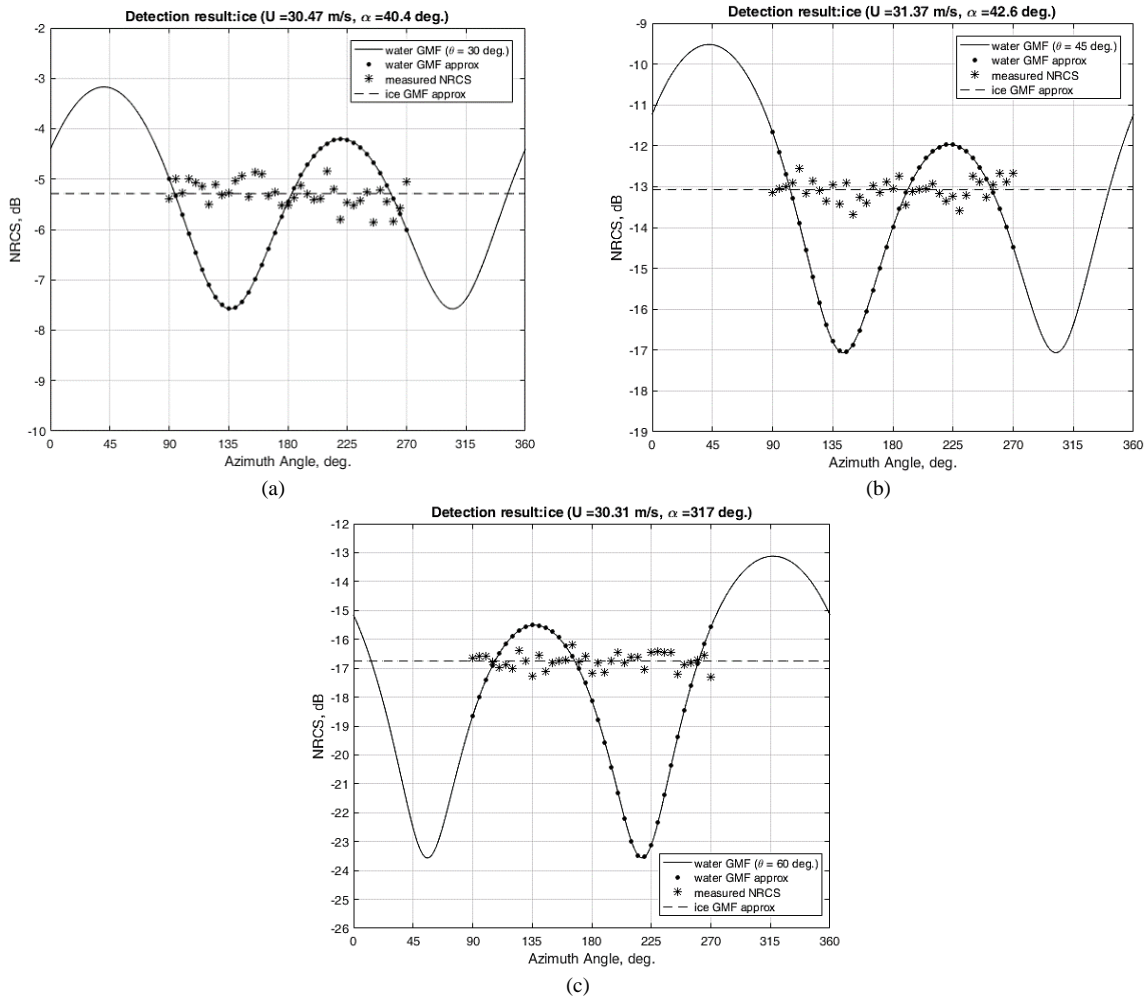


**Figure 11.** Sea ice surface simulation results at 30 m/s wind speed and various incidence angles: (a) 30°; (b) 45°; (c) 60°;  $U$  is the wind speed;  $\alpha$  is the upwind direction; and  $\theta$  is the incidence angle

The summation results obtained for the sea ice surface scenario, with the help of Equations 5 and 6, are presented in Table 3. The discrimination reliability indicators in this scenario are the ratios of the sea water and ice summation results in the sea ice surface scenario and are given in Table 4.

**Table 3.** Sea ice surface scenario summation results

Related wind speed	Summation result	Incidence angle		
		30°	45°	60°
2 m/s	$S_{\approx}$	$1.71443 \cdot 10^{-5}$	$1.88241 \cdot 10^{-8}$	$5.15423 \cdot 10^{-10}$
	$S_{\equiv}$	$1.14582 \cdot 10^{-6}$	$1.39398 \cdot 10^{-9}$	$2.91 \cdot 10^{-11}$
10 m/s	$S_{\approx}$	$3.87488 \cdot 10^{-3}$	$5.2453 \cdot 10^{-5}$	$5.70371 \cdot 10^{-6}$
	$S_{\equiv}$	$3.44301 \cdot 10^{-4}$	$3.48309 \cdot 10^{-6}$	$2.1477 \cdot 10^{-7}$
20 m/s	$S_{\approx}$	$4.93752 \cdot 10^{-2}$	$1.19843 \cdot 10^{-3}$	$3.05762 \cdot 10^{-4}$
	$S_{\equiv}$	$4.35806 \cdot 10^{-3}$	$4.77531 \cdot 10^{-5}$	$4.84779 \cdot 10^{-6}$
30 m/s	$S_{\approx}$	0.16319	$9.62547 \cdot 10^{-3}$	$2.91891 \cdot 10^{-3}$
	$S_{\equiv}$	$1.09542 \cdot 10^{-2}$	$3.02996 \cdot 10^{-4}$	$6.14618 \cdot 10^{-5}$

**Table 4.** Sea water/ice summation results' ratios in the sea ice surface scenario

Water/sea ice summation results' ratios	Wind speed	Incidence angle		
		30°	45°	60°
	2 m/s	14.96	13.5	17.71
	10 m/s	11.25	15.06	26.56
	20 m/s	11.33	25.1	63.07
	30 m/s	14.9	31.77	47.49

These results show well the closer fit of the “measured” semicircular NRCSs (asterisks in Figures 8 to 11) to the approximated line of the sea ice GMF (dashed line) than to the curve of the sea water GMF (solid line) at the considered incidence angles and related speeds of the sea wind in the case of a sea ice surface scenario, and so the underlying surface is correctly recognized as sea ice by the discrimination method via Equation 7. Table 4 shows that the sea water and ice summation results’ ratios significantly exceed the value of 1, and they increase in general with an increase in the incidence angle, again showing the preferability of incidence angles higher than 30° for sea water/ice discrimination (within the considered incidence angles of 30°, 45°, and 60°).

### 3-3- Results Summary

Summarizing the presented simulation results within both scenarios, we can conclude that for all considered values of incidence angles and wind speeds, it is clear that in the case of a sea water scenario, the measured NRCS values coincide much better with the shape of the sea water GMF’s azimuthal curve than with the shape of the sea ice GMF’s (approximated) straight line, while in the case of a sea ice scenario, the measured NRCS values coincide much better with the shape of the sea ice GMF’s line than with the shape of the sea water GMF’s azimuthal curve.

As the difference in the azimuth shape between the sea water NRCS curve and sea ice NRCS line is crucial for sea water/ice discrimination by a conical scanning scatterometer, it is essential to provide the largest difference between their shapes. As the sea ice NRCS is an azimuth isotropic curve [40] that looks something like a straight line, the difference is primarily determined by the azimuth shape of the sea water NRCS curve (sea water GMF). From Figures 3 to 6 and 8 to 11, we can see that the difference between the main maximum and minima of the sea water GMF depends on the incidence angle and wind speed. For the simulation results, depending on the sea wind speed, the difference is about 4.0–4.5 dB, 6.5–7.5 dB, and 7.0–10.5 dB, respectively, at incidence angles of 30°, 45°, and 60°. Thus, the lowest difference corresponds to the lowest sea wind speed of 2 m/s at the lowest incidence angle of 30° and increases with an increase in the incidence angle and sea wind speed. Therefore, this difference can be fully used in the circular observation scheme and at incidence angles tending to 60°.

However, in the case of our semicircular observation scheme, the main maximum and at least one minimum may not always be within the observed azimuth semicircle, so this peculiarity must be taken into consideration. Accordingly, our simulations were performed for the worst case of the semicircular sea water observation with observed azimuths from 90° to 270° characterized by the lowest difference between values of the second maximum and minima of the sea water azimuth’s NRCS curve. This value is decisive in providing sea water/ice discrimination using semicircular observations. Depending on the sea wind speed, the considered difference in this worst case of semicircular observations is somewhat lower than in the case of circular observations, being about 2.5–3.5 dB, 2.5–5.0 dB, and 3.0–8.0 dB, at incidence angles of 30°, 45°, and 60°, respectively.

Thus, a semicircular observation scheme may be slightly worse at providing the difference in the azimuth shape between the sea water NRCS curve and sea ice NRCS line than a circular observation scheme. Nonetheless, our simulations showed that a semicircular observation scheme combined with our sea water/ice discrimination criterion works well in both sea water and ice scenarios for all considered combinations of incidence angles and wind speeds, as is clearly visible in Figures 3 to 6 and 8 to 11. This outcome is also confirmed by the sea water/ice discrimination indicators, which are much higher than 1 in the appropriate surface scenarios. Table 2 shows that the ratio of the sea ice/water summation results varies from 9.41 to 71.73 depending on the incidence angle and sea wind speed in a sea water surface scenario, and Table 4 demonstrates that the ratio of the sea water/ice summation results varies from 11.25 to 63.07 depending on the incidence angle and sea wind speed in a sea ice surface scenario. Thus, we can see that even at an incidence angle of 30°, the indicators are about 10 times higher than 1, and their further increase with increase of the incidence angle proves the feasibility of our semicircular observation scheme, the sea water/ice discrimination method, and its applicability for a high-altitude conical scanning radar operated in scatterometer mode.

The results in Figures 3 to 6 and 8 to 11 also prove the applicability of our decision to use a substitute sea ice GMF for the shape of the NRCS azimuth line, given that no suitable sea ice GMF is available (or even known). This substitute sea ice GMF has an isotropic azimuth property, and its value is assumed to be equal to the averaged value of the measured azimuth NRCSs within the semicircular observation scheme, which is considered similar to the real sea ice GMF and is sufficient to perform sea water/ice discrimination when a sea ice surface is observed. Of course, if sea water is observed, the value of such a substitute sea ice GMF has nothing in common with the value of the real sea ice GMF, but the substitute sea ice GMF azimuth isotropic properties will still be similar to the real sea ice GMF and can also be successfully used to perform sea water/ice discrimination within a semicircular observation scheme.

Recently, we have shown that a semicircular observation scheme allows doubling the maximum altitude of sea wind retrieval compared to a circular observation scheme [26, 27]. Therefore, since sea wind retrieval is an integral part of the sea water/ice discrimination procedure, a semicircular observation scheme also doubles the maximum altitude of the sea water/ice discrimination method for a high-altitude conical scanning radar. The maximum altitude limitations for semicircular observations are about 34.6, 20, and 11.54 km at the incidence angles of 30°, 45°, and 60°, respectively. In contrast to this advantage of semicircular observations, the maximum altitude limitations for circular observations were only 17.3, 10, and 5.77 km at incidence angles of 30°, 45°, and 60° [26, 27].

The results obtained in Figures 8 to 11 also demonstrate the need to implement the sea water/ice discrimination procedure for any airborne wind scatterometer or multimode radar operated in scatterometer mode over freezing seas because their operation over a sea ice surface without such a discrimination option will cause absolutely erroneous results for the sea wind speed and direction. We have also demonstrated in these figures how application of the sea wind retrieval method based on Equations 1 to 3 to sea ice surface observations can result in an arbitrarily wrong wind direction (the given upwind direction was always set to  $0^\circ$  during the simulations).

The NRCS observations should be performed at a constant incidence angle within the observation scheme, and so the antenna of the high-altitude conical scanning radar should be stabilized in the horizontal plane. To start the measurements, a stable horizontal rectilinear flight with a constant altitude and speed of flight should be established. It is necessary to maintain the consistency of the flight parameters during the observations. The measurements are terminated after obtaining the required number of NRCSs for each azimuth sector.

## 4- Conclusion

This study analyzed the ability to enhance airborne high-altitude conical scanning radar functionality to perform sea water/ice discrimination in addition to its typical cloud and precipitation observations as well as wind measurements. To increase the maximum altitude of the sea water/ice discrimination method, a semicircular observation scheme was applied instead of a circular observation, and this allowed the altitude to be doubled. The sea water/ice discrimination method was based on the minimum statistical distance of measured NRCSs to the sea water and ice GMFs. As a sea ice GMF is unavailable at a Ku-band, we instead substituted the unknown sea ice GMF by the NRCS azimuth line, whose value was defined as the average of the measured azimuth NRCSs within the semicircular observation scheme. Although the value of this substitute sea ice GMF likely differs from the actual but unknown sea ice GMF, it nonetheless has the same azimuth isotropic property, which, as we showed herein, is still sufficient to perform sea water/ice discrimination.

All the considered incidence angles of  $30^\circ$ ,  $45^\circ$ , and  $60^\circ$  are well suited to sea water/ice discrimination, although incidence angles higher than  $30^\circ$  are preferable because they provide a higher difference in the statistical distance of the measured NRCSs between the sea ice and water GMFs, while the  $30^\circ$  incidence angle provides the highest maximum altitude of the sea water/ice discrimination and wind retrieval. The maximum altitude limitations for semicircular observations are about 34.6, 20, and 11.54 km at the appropriate incidence angles of  $30^\circ$ ,  $45^\circ$ , and  $60^\circ$ , respectively. These maximum altitudes in the semicircular scheme are double those of circular observations. Our study also showed an urgent need to implement the sea water/ice discrimination option for any airborne wind scatterometer or multimode radar operated in the scatterometer mode over freezing seas, because their application over sea ice patches without such a sea water/ice discrimination option can give wholly erroneous sea wind measurement results. These research outcomes can contribute to oceanography, meteorology, and navigation applications, the enhancement of aircraft and UAV radars, and the development of new remote sensing systems.

## 5- Declarations

### 5-1- Author Contributions

Conceptualization, A.N.; methodology, A.N., A.K., and C.F.; software, A.K.; validation, A.N., A.K., and C.F.; formal analysis, A.N. and A.K.; investigation, A.N., A.K., and C.F.; resources, A.K.; data curation, A.N. and A.K.; writing—original draft preparation, A.N.; writing—review and editing, A.N., A.K., and C.F.; visualization, A.N. and A.K.; supervision, A.N.; project administration, A.K.; funding acquisition, A.K. All authors have read and agreed to the published version of the manuscript.

### 5-2- Data Availability Statement

The data presented in this study are available on request from the corresponding author.

### 5-3- Funding

This research was funded by the Russian Science Foundation grant number 21-79-10375, <https://rscf.ru/en/project/21-79-10375/> (accessed on 12 March 2023). The APC was funded by the Russian Science Foundation grant number 21-79-10375.

### 5-4- Institutional Review Board Statement

Not applicable.

### 5-5- Informed Consent Statement

Not applicable.

### 5-6- Conflicts of Interest

The authors declare that there is no conflict of interest regarding the publication of this manuscript. In addition, the ethical issues, including plagiarism, informed consent, misconduct, data fabrication and/or falsification, double publication and/or submission, and redundancies have been completely observed by the authors.

### 6- References

- [1] Wikipedia. (2024). Measurement of sea ice. Available online: [https://en.wikipedia.org/wiki/Measurement\\_of\\_sea\\_ice](https://en.wikipedia.org/wiki/Measurement_of_sea_ice) (accessed on March 2024).
- [2] Njoku, E. G. (2014). *Encyclopedia of Remote Sensing*. Springer, New York, United States. doi:10.1007/978-0-387-36699-9.
- [3] Johannessen, O. M., Alexandrov, V., Frolov, I. Y., Sandven, S., Pettersson, L. H., Bobylev, L. P., Kloster, K., Smirnov, V. G., Mironov, Y. U., & Babich, N. G. (2007). *Remote Sensing of Sea Ice in the Northern Sea Route: Studies and Applications*. Springer, Berlin/Heidelberg, Germany. doi:10.1007/978-3-540-48840-8.
- [4] Sandven, S., Spreen, G., Heygster, G., Girard-Ardhuin, F., Farrell, S. L., Dierking, W., & Allard, R. A. (2023). Sea Ice Remote Sensing—Recent Developments in Methods and Climate Data Sets. *Surveys in Geophysics*, 44(5), 1653–1689. doi:10.1007/s10712-023-09781-0.
- [5] Gabarró, C., Hughes, N., Wilkinson, J., Bertino, L., Bracher, A., Diehl, T., Dierking, W., Gonzalez-Gambau, V., Lavergne, T., Madurell, T., Malnes, E., & Wagner, P. M. (2023). Improving satellite-based monitoring of the Polar Regions: Identification of research and capacity gaps. *Frontiers in Remote Sensing*, 4. doi:10.3389/frsen.2023.952091.
- [6] Yang, Z., Yu, X., Dedman, S., Rosso, M., Zhu, J., Yang, J., Xia, Y., Tian, Y., Zhang, G., & Wang, J. (2022). UAV remote sensing applications in marine monitoring: Knowledge visualization and review. *Science of the Total Environment*, 838, 155939. doi:10.1016/j.scitotenv.2022.155939.
- [7] Yuan, S., Li, Y., Bao, F., Xu, H., Yang, Y., Yan, Q., Zhong, S., Yin, H., Xu, J., Huang, Z., & Lin, J. (2023). Marine environmental monitoring with unmanned vehicle platforms: Present applications and future prospects. *Science of the Total Environment*, 858, 159741. doi:10.1016/j.scitotenv.2022.159741.
- [8] Håheim-Saers, N. (2022). Arctic UAS study. Arctic threats to safe design of Unmanned Aerial Systems. Report No. 2-2022, NORCE Energy & Technology, Bergen, Norway.
- [9] Mersmann, K. (2022). NASA is Helping Fly Drones in the Arctic. Here's what that Means for Sea Ice and Sea Level Change. The National Aeronautics and Space Administration (NASA), Washington, United States. Available online: <https://www.nasa.gov/feature/goddard/2022/nasa-helps-fly-drone-in-alaska-to-study-sea-ice-thickness> (accessed on March 2024).
- [10] Li, L., Heymsfield, G., Carswell, J., Schaubert, D. H., McLinden, M. L., Creticos, J., Perrine, M., Coon, M., Cervantes, J. I., Vega, M., Guimond, S., Tian, L., & Emory, A. (2016). The NASA High-Altitude Imaging Wind and Rain Airborne Profiler. *IEEE Transactions on Geoscience and Remote Sensing*, 54(1), 298–310. doi:10.1109/TGRS.2015.2456501.
- [11] NASA. (2023). High-Altitude Radar. Goddard Space Flight Center. The National Aeronautics and Space Administration (NASA), Washington, United States. Available online: <https://har.gsfc.nasa.gov/index.php?section=13> (accessed on March 2024).
- [12] Guimond, S. R., Tian, L., Heymsfield, G. M., & Frasier, S. J. (2014). Wind retrieval algorithms for the IWRAP and HIWRAP airborne doppler radars with applications to hurricanes. *Journal of Atmospheric and Oceanic Technology*, 31(6), 1189–1215. doi:10.1175/JTECH-D-13-00140.1.
- [13] Moore, R. K. (1985). Radar Sensing of the Ocean. *IEEE Journal of Oceanic Engineering*, 10(2), 84–113. doi:10.1109/JOE.1985.1145093.
- [14] Masuko, H., Okamoto, K., Shimada, M., & Niwa, S. (1986). Measurement of microwave backscattering signatures of the ocean surface using X band and Ka band airborne scatterometers. *Journal of Geophysical Research: Oceans*, 91(C11), 13065–13083. doi:10.1029/jc091ic11p13065.
- [15] Carswell, J. R., Carson, S. C., McIntosh, R. E., Li, F. K., Neumann, G., McLaughlin, D. J., Wilkerson, J. C., Black, P. G., & Nghiem, S. V. (1994). Airborne scatterometers: investigating ocean backscatter under low- and high-wind conditions. *Proceedings of the IEEE*, 82(12), 1835–1860. <https://doi.org/10.1109/5.338074>.
- [16] Nekrasov, A., Khachaturian, A., Abramov, E., Popov, D., Markelov, O., Obukhovets, V., Veremyev, V., & Bogachev, M. (2018). Optimization of airborne antenna geometry for ocean surface scatterometric measurements. *Remote Sensing*, 10(10), 1501. doi:10.3390/rs10101501.
- [17] Nekrasov, A., & Khachaturian, A. (2021). Towards the Sea Wind Measurement with the Airborne Scatterometer Having the Rotating-Beam Antenna Mounted over Fuselage. *Remote Sensing*, 13(24), 5165. doi:10.3390/rs13245165.

- [18] Nekrasov, A., Khachaturian, A., & Vorobev, E. (2022). Optimization of the NRCS Sampling at the Sea Wind Retrieval by the Airborne Rotating- Beam Scatterometer Mounted under Fuselage. *Sensors*, 22(11), 4016. doi:10.3390/s22114016.
- [19] Nekrasov, A., de Wit, J. J. M., & Hoogeboom, P. (2004). FM-CW millimeter wave demonstrator system as a sensor of the sea surface wind vector. *IEICE Electronics Express*, 1(6), 137–143. doi:10.1587/elex.1.137.
- [20] Nekrasov, A. (2010). Airborne Doppler navigation system application for measurement of the water surface backscattering signature. *ISPRS TC VII Symposium—100 Years ISPRS*, 5–7 July, 2010, Vienna, Austria.
- [21] Nekrasov, A. (2005). Measuring the sea surface wind vector by the Doppler navigation system of flying apparatus having the track-stabilized four-beam antenna. 17<sup>th</sup> Asia Pacific Microwave Conference (APMC), Suzhou, China, 4–7 December, 2005. doi:10.1109/APMC.2005.16063433.
- [22] Nekrasov, A., & Dell'Acqua, F. (2016). Airborne Weather Radar: A theoretical approach for water-surface backscattering and wind measurements. *IEEE Geoscience and Remote Sensing Magazine*, 4(4), 38–50. doi:10.1109/MGRS.2016.2613840.
- [23] Nekrasov, A., & Veremyev, V. (2016). Airborne Weather Radar Concept for Measuring Water Surface Backscattering Signature and Sea Wind at Circular Flight. *Naše More*, 63(4), 278–282. doi:10.17818/nm/2016/4.5.
- [24] Wikipedia. (2024). Flight altitude record. Available online: [https://en.wikipedia.org/wiki/Flight\\_altitude\\_record](https://en.wikipedia.org/wiki/Flight_altitude_record) (accessed on March 2024).
- [25] Holland Michel, A. (2015). Bard College Center for the Study of the Drone, Bard College, Red Hook, United States. Available online: <https://dronecenter.bard.edu/high-altitude-drones> (accessed on March 2024).
- [26] Nekrasov, A., Khachaturian, A., & Fidge, C. (2022). Using Semicircular Sampling to Increase Sea-Wind Retrieval Altitude with a High-Altitude UAV Scatterometer. *Drones*, 6(9), 223. doi:10.3390/drones6090223.
- [27] Nekrasov, A., Khachaturian, A., & Fidge, C. (2023). Optimization of Airborne Scatterometer NRCS Semicircular Sampling for Sea Wind Retrieval. *Remote Sensing*, 15(6), 1613. doi:10.3390/rs15061613.
- [28] Nekrasov, A., Khachaturian, A., Abramov, E., Kurdel, P., Gamcova, M., Gamec, J., & Bogachev, M. (2020). On Sea Ice/Water Discrimination by Airborne Weather Radar. *IEEE Access*, 8, 120916–120922. doi:10.1109/ACCESS.2020.3006617.
- [29] Nekrasov, A., Khachaturian, A., Abramov, E., Markelov, O., & Bogachev, M. (2019). On sea ice measurement by a C-band scatterometer at VV polarization: Methodology optimization based on computer simulations. *Remote Sensing*, 11(21), 2518. doi:10.3390/rs11212518.
- [30] Nekrasov, A., Khachaturian, A., Labun, J., Kurdel, P., & Bogachev, M. (2020). Towards the Sea Ice and Wind Measurement by a C-Band Scatterometer at Dual VV/HH Polarization: A Prospective Appraisal. *Remote Sensing*, 12(20), 3382. doi:10.3390/rs12203382.
- [31] Nekrasov, A., Khachaturian, A., Veremyev, V., & Bogachev, M. (2016). Sea surface wind measurement by airborne weather radar scanning in a wide-size sector. *Atmosphere*, 7(5), 72. doi:10.3390/atmos7050072.
- [32] Spencer, M. W. (1997). The NASA scatterometer (NSCAT) mission. *Backscatter*, 8(4), 18–24.
- [33] Hans, P. (1987). Design and analysis of satellite-borne microwave sensor systems for wind field measurement (scatterometer) over the sea and comparison of the measurement methods in time and frequency levels. Ph.D. Thesis, Universität Stuttgart, Stuttgart, Germany. (In German).
- [34] Nekrasov, A. (1999). Sea surface wind vector measurement by airborne scatterometer having wide-beam antenna in horizontal plane. *International Geoscience and Remote Sensing Symposium IGARSS'99*, 28 June – 02 July 1999, Hamburg, Germany. 1001–1003. doi:10.1109/IGARSS.1999.774512.
- [35] Nekrasov, A. (2002). On airborne measurement of the sea surface wind vector by a scatterometer (altimeter) with a nadir-looking wide-beam antenna. *IEEE Transactions on Geoscience and Remote Sensing*, 40(10), 2111–2116. doi:10.1109/TGRS.2002.803621.
- [36] Nekrasov, A., Khachaturian, A., Veremyev, V., & Bogachev, M. (2017). Doppler navigation system with a non-stabilized antenna as a sea-surface wind sensor. *Sensors*, 17(6), 1340. doi:10.3390/s17061340.
- [37] Ulaby, F., & Long, D. (2014). *Microwave Radar and Radiometric Remote Sensing*. Artech House, Norwood, United States. doi:10.3998/0472119356.
- [38] Belmonte Rivas, M., Verspeek, J., Verhoef, A., & Stoffelen, A. (2012). Bayesian Sea Ice Detection with the Advanced Scatterometer ASCAT. *IEEE Transactions on Geoscience and Remote Sensing*, 50(7), 2649–2657. doi:10.1109/tgrs.2011.2182356.
- [39] Otsuka, I., Rivas, M. B., & Stoffelen, A. (2018). Bayesian sea ice detection with the ERS scatterometer and sea ice backscatter model at C-band. *IEEE Transactions on Geoscience and Remote Sensing*, 56(4), 2248–2254. doi:10.1109/TGRS.2017.2777670.

- [40] Frey, K. E., Smith, L. C., & Alsdorf, D. E. (2003). Controls on Eurasian coastal sea ice formation, melt onset and decay from ERS scatterometry: Regional contrasts and effects of river influx. *International Journal of Remote Sensing*, 24(24), 5283–5315. doi:10.1080/0143116031000101684.
- [41] KNMI Projects. (2024). *Globe Educatieprojecten: CMOD7*. Royal Netherlands Meteorological Institute, De Bilt, Netherlands. Available online: <http://projects.knmi.nl/scatterometer/cmod7> (accessed on March 2024).
- [42] Otsuka, I., Rivas, M. B., & Stoffelen, A. (2019). Errata: Bayesian sea ice detection with the ERS scatterometer and sea ice backscatter model at C-band. *IEEE Transactions on Geoscience and Remote Sensing*, 57(12), 10447-10447. doi:10.1109/TGRS.2019.2928720.
- [43] Alpers, W., Zhang, B., Mouche, A., Zeng, K., & Chan, P. W. (2016). Rain footprints on C-band synthetic aperture radar images of the ocean - Revisited. *Remote Sensing of Environment*, 187, 169–185. doi:10.1016/j.rse.2016.10.015.
- [44] Xu, X., Stoffelen, A., Ni, W., Portabella, M., & Rabaneda, A. (2023). Extreme Winds from Ku-Band and C-Band Wind Scatterometers. *IGARSS 2023 - 2023 IEEE International Geoscience and Remote Sensing Symposium*, California, United States. doi:10.1109/igarss52108.2023.10281803.
- [45] Komen, G. J., Cavaleri, L., Donelan, M., Hasselmann, K., Hasselmann, S., & Janssen, P. A. E. M. (1994). *Dynamics and Modelling of Ocean Waves*. Cambridge University Press, Cambridge, United Kingdom. doi:10.1017/cbo9780511628955.